

# A statistical study of Lopsided Galaxies using Random Forests

Valentina Fontirroig<sup>1</sup>, Facundo A. Gómez<sup>1</sup>, Marcelo Jaque Arancibia<sup>1</sup>, Arianna Dolfi<sup>1</sup>, and  
Nicolás Monsalves<sup>1</sup>

<sup>1</sup> Departamento de Astronomía, Universidad de La Serena, av. Raul Bitran, La Serena, Chile  
e-mail: valentina.fontirroig@userena.cl

December 2, 2024

## ABSTRACT

*Context.* Lopsided galaxies are late-type galaxies that feature a non-axisymmetric disc caused by an uneven distribution of their stellar mass, or light. Despite being a relatively common perturbation, several questions regarding its origin, and the information that can be extracted from them about the evolutionary history of late-type galaxies.

*Aims.* The advent of several large multi-band photometric surveys will allow us to statistically analyze this perturbation, with information that was not previously available. Given the strong correlation between lopsidedness and the structural properties of the galaxies, this paper aims to develop a method to automatically classify late-type galaxies between lopsided and symmetric. We seek to explore whether an accurate classification can be obtained by only considering their internal properties, without additional information regarding the environment inhabited by the galaxies.

*Methods.* We select a sample of  $\approx 8,000$  late type galaxies from the Illustris TNG50 simulation. A Fourier decomposition of their stellar mass surface density is used to label galaxies as lopsided and symmetric. We trained a Random Forest classifier to rapidly and automatically identify this type of perturbations, exclusively using galaxies internal properties. We explore different algorithms to deal with the imbalance nature of our data, and select the most suitable approach based on the considered metrics.

*Results.* We show that our trained algorithm can provide a very accurate and rapid classification of lopsided galaxies. The excellent results obtained by our classifier, trained with features that do not account for the galaxies environment, strongly supports the hypothesis that lopsidedness is mainly a tracer of galaxies internal structures. We also show that similar results can be obtained when considering as input features observable quantities that are readily obtainable from multi-band photometric surveys.

*Conclusions.* Our results show that algorithms such as those considered allow a rapid and accurate classification of lopsided galaxies from large multi-band photometric surveys, allowing us to explore whether lopsidedness in present-day disc galaxies is connected to galaxies specific evolutionary histories.

**Key words.** Galaxies: evolution – Galaxies: formation – Galaxies: spiral – Galaxies: structure – Methods: data analysis – Methods: statistical

## 1. Introduction

Lopsided galaxies feature a non-axisymmetric disc, caused by an uneven distribution of stellar mass or light. Observational studies have shown that up to 30% of nearby galaxies display certain degree of lopsidedness (Zaritsky & Rix 1997; Rudnick & Rix 1998; Bournaud et al. 2005; van Eymeren et al. 2011). The term "lopsidedness" was first coined by Baldwin et al. (1980) to refer to those galaxies in their sample that show a strong asymmetry in the HI gas density distribution between their two opposite sides. As discussed in Jog & Combes (2009, and references therein), this asymmetry can significantly impact the dynamical structure and evolution of the host galaxy, causing enhanced star forming regions, fueling the central active galactic nucleus, and redistributing matter, among others.

Despite lopsided galaxies being an ubiquitous object in the nearby universe, this asymmetry has received less attention than other commonly studied perturbations (e.g. Sellwood 2013; Conselice 2014; Erwin 2019). Moreover, the origin of this asymmetry is not quite well understood, as both galaxies in the field and in denser environment present lopsidedness. Different mechanisms have been proposed as the main driver of this asymmetry, such as asymmetric gas accretion (Phookun et al. 1993; Bournaud et al. 2005), tidal encounters (Weinberg 1994; Rudnick et al. 2000; Gómez et al. 2016), satellite accretion (Walker et al.

1996; Zaritsky & Rix 1997), response of the disc to the distorted dark matter halo (Jog 1997, 2002), and off-centered disc (Noor-dermeer et al. 2001), among others.

Interestingly, several works have also found that lopsided galaxies show differences in their structural properties with respect to more symmetrical late-type galaxies. In particular, Reichard et al. (2008) studied a sample of 25,155 low redshift ( $z < 0.06$ ) galaxies in the Sloan Digital Sky Survey (SDSS, Kollmeier et al. 2019), and showed that lopsided galaxies tend to have lower concentration and stellar mass density within their half light radius than symmetrical galaxies. This suggests that there is a correlation between lopsidedness and the structural properties of the galaxies. Using a sample of late-type galaxies from the Illustris TNG50 simulation, Varela-Lavin et al. (2023) found a similar strong correlation between lopsidedness and the internal properties of galaxies. Specifically, they found an anti-correlation between lopsidedness and the tidal force exerted by the inner regions on the outskirts of their galactic disc. This result indicates that less gravitationally cohesive disk galaxies are more susceptible to develop this asymmetry when exposed to external perturbations. Dolfi et al. (2023) extended this study by considering a larger sample of  $z = 0$  TNG50 disc-like galaxies, located in different environments. They showed that, independently of the environment, while symmetric galaxies are typically assem-

bled at early times ( $\sim 8 - 6$  Gyr ago), with a relatively short and intense burst of central star formation, lopsided galaxies assembled over a longer time period, with less prominent initial bursts and a subsequent milder and constant star formation rate up to  $z = 0$ .

Current and upcoming large observational surveys, such as S-Plus (Mendes de Oliveira et al. 2019), J-Plus (Cenarro et al. 2019), J-PAS (Benitez et al. 2014), and LSST (Ivezić et al. 2019), will enable to identify and characterize lopsidedness in a very large number of well-resolved galaxies in the local Universe. This will be crucial to further study the connection between such perturbation and the galaxy internal properties, and to test current model predictions and understand the origin of lopsidedness considering their star formation history in relation with the environment. However, as the volume of data increases, using traditional approaches to study and characterize this non-axisymmetry, such as visual inspection (e.g. Baldwin et al. 1980; Richter & Sacisi 1994), identification of surface brightness residuals with respect to unperturbed distributions (e.g. Conselice et al. 2000) and Fourier decomposition (e.g. Zaritsky & Rix 1997; Reichard et al. 2008), can become a limiting task. All these techniques require human supervision and intervention (such as visual inspection) and, thus result in cumbersome and slow approach to study lopsidedness in larger volumes of data, which could also result in missing important information or discoveries.

To avoid this problem, machine learning algorithms are a helpful tool used to automate and speed up the classification of objects such as galaxies. Different algorithms can be used for different tasks depending on the problem to solve. For example, some methods are defined as supervised, as they require a subsample of already labeled data to train and test a model (generally referred as training set). A few of these algorithms consist of ensemble methods (Random Forests (Breiman 2001) and Gradient Boosting (Friedman 2001)), artificial neural networks (Convolutional Neural Networks (O’Shea & Nash 2015) and Recurrent Neural Networks (Rumelhart & McClelland 1987)), distance-based algorithms (Nearest Neighbors algorithms (Cover & Hart 1967)), among others. Some examples of their application are morphological classification of galaxies (Ball et al. 2004; Dieleman et al. 2015; Huertas-Company et al. 2015; Farias et al. 2020), classification of variable stars using time-domain (Aguirre et al. 2019; Monsalves et al. 2024), and the estimation of photometric redshifts (Zhang et al. 2013; Lee & Shin 2021). On the other hand, unsupervised algorithms such as clustering (k-means (Lloyd 1982) and Hierarchical clustering (Guha et al. 2000)) and dimensional reduction algorithms (Principal Component Analysis (Jolliffe 2002)), are trained with unlabeled data. They are typically employed for anomaly detection (Hocking et al. 2018; Giles & Walkowicz 2019; Sarkar et al. 2022), feature selection (Cheng et al. 2020) and extraction (Baron & Poznanski 2017), and even galaxy classification (Hocking et al. 2018).

Given the previously reported strong correlation between lopsidedness and the structural properties of galaxies, this paper aims at using machine learning techniques to automatically classify galaxies between lopsided and symmetric by only using their internal properties. We also seek to explore whether an accurate classification of this asymmetry can be obtained without including any direct information regarding the environment inhabited by the galaxies. Our selected machine learning algorithms will be trained and tested over a large sample of galaxies obtained from the IllustrisTNG simulation. We will also determine the key parameters that allow the correct classification of

lopsided galaxies. The organization of this paper is as follows: In Sect. 2 we list the selection criteria to obtain the internal and observational parameters of disc-like galaxies extracted from the TNG50-1 simulation. In Sect. 3 we describe the procedure we follow to implement the classification algorithms. In Sect. 4 we list and analyze our results. The conclusions and discussion are finally presented in Sect. 5.

## 2. Data

In this section, we present the criteria to select the necessary dataset to train and test our selected classification models, discussed in Sect. 3.2. In particular, we use galaxy models extracted from the fully cosmological simulation, IllustrisTNG50 (Nelson et al. 2019a; Pillepich et al. 2019a). For each galaxy model, we compute internal parameters that are commonly measured in observational studies to classify galaxies’ morphology.

### 2.1. The IllustrisTNG project

IllustrisTNG (hereafter TNG), successor of the Illustris project (Genel et al. 2014; Vogelsberger et al. 2014; Nelson et al. 2015), is a set of cosmological, gravo-magnetohydrodynamical simulation, ran with the moving-mesh code AREPO (Springel 2010). IllustrisTNG builds upon its predecessor model (Genel et al. 2014) by incorporating an updated physical model (Pillepich et al. 2018) which accounts for stellar evolution, gas cooling, feedback and growth from supermassive blackholes, among others. In particular, the improved model for the feedback of the low accretion mode in super massive black holes resulted in a reduction of the discrepancies with observational constraints identified in the original Illustris simulations, such as the galaxy color bimodality (Nelson et al. 2018). These improvements make IllustrisTNG a powerful tool for comparisons with observational data.

TNG consists of three simulations with different volumes:  $50^3\text{Mpc}$ ,  $100^3\text{Mpc}$  and  $300^3\text{Mpc}$ , referred as TNG50, TNG100, and TNG300, respectively. Each simulation was run with different mass and spatial resolution. As a result, the three realizations complement each other. For example, the largest simulation box, TNG300, enables the study of galaxy clustering and provides the largest statistical galaxy sample. On the other hand, TNG50 provides the smallest galaxy sample at the high mass end, but it has the highest mass resolution overall. Therefore, it enables a more detailed look at the morphology of galaxies and its structural properties. TNG-100 falls somewhere in between these two other simulations.

In this work, due to its mass and spatial resolution, we make use of the publicly available TNG50-1 model (Pillepich et al. 2019b; Nelson et al. 2019b). Having a dark matter, baryonic mass resolution of  $4.5 \times 10^5 M_\odot$ , and  $8.5 \times 10^4 M_\odot$ , respectively, TNG50-1 allow us to resolve the structure of  $10^9 M_\odot$  stellar disc with at least  $10^4$  stellar particles, enabling a better characterization of their morphology (Nelson et al. 2019c).

The cosmological model adopted in IllustrisTNG is a flat  $\Lambda$ CDM universe with the following parameters: Hubble constant  $H_0 = 67.8 \text{ km s}^{-1} \text{ Mpc}^{-1}$ , total matter density  $\Omega_m = 0.3089$ , dark energy density  $\Omega_\Lambda = 0.6911$ , baryonic matter density  $\Omega_b = 0.8159$ , rms of mass fluctuations at a scale of  $8 h^{-1} \text{ Mpc}$   $\sigma_8 = 0.8159$  and a primordial spectral index  $n_s = 0.9667$  (Planck Collaboration et al. 2016).

**Table 1.** List of the internal parameters of the 7,919 disc-like galaxies obtained from TNG50-1.

Parameters	Symbol	Description
Tidal Parameter <sup>1</sup>	$T_P$	Represents the tidal force applied by the inner galaxy regions ( $R < R_{50}$ ) to the materials located at distances equal to $R_{90}$ . Defined as $T_P = M_{50}^{\text{tot}}/R_{90}^3$ . Here $M_{50}^{\text{tot}}$ represent the total (baryonic + DM) mass within $R_{50}$ .
Central Stellar Mass Density	$\mu_*$	Density of the stellar mass contained inside $R_{50}$ . Defined as $\mu_{star} = M_{50}/\pi R_{50}^2$ .
Minor-to-major axis	$c/a$	Ratio between the minor axis $c$ and major axis $a$ . Describes the shape of the inner galactic regions.
disc-to-total mass	$D/T$	Ratio between the disc's mass and the total mass of the galaxy. Used to select disc-like galaxies.
Concentration	$C$	Ratio between $R_{90}$ and the effective radius $R_{50}$ . Defined as $C = R_{90}/R_{50}$ .
Effective Radius	$R_{50}$	Radius of the galaxy containing 50% of the stellar mass.
Disc Extension	$R_{\text{ext}}$	Defined as 1.4 times the radius of the galaxy containing 90% of the stellar mass ( $R_{90}$ ).
Half-mass	$M_{50}$	Stellar mass of the galaxy enclosed in $R_{50}$ .
Star Formation Rate	$SFR$	Total stellar mass created from gas and dust, per year.
Spin Parameter <sup>1</sup>	$\Lambda(R)$	Galactic disc stellar spin, which is a proxy of the apparent stellar angular momentum. Calculated within the inner stellar half-mass radius.

**References.** (1) Lagos et al. (2017).

## 2.2. Selection Criteria

We will focus our study on central and satellite disc-like galaxies, identified within the redshift range  $z=0$  to  $z=0.5$ . The  $z$  range considered allow us to obtain a large number of galaxy models to train our classification algorithm. Note that, even though a given galaxy will be present at different snapshots of the simulation, their detailed structure will evolve (see e.g. Varela-Lavin et al. 2023) and, thus, it will serve as input for the training process.

Following Dolfi et al. (2023) based on our selection criteria, we consider galaxies with:

- $N_{\text{tot,stars}} \geq 10^4$ , where  $N_{\text{tot,stars}}$  represents the number of bound stellar particles. This is used to make sure that galaxies have enough stellar particles to be reasonably well resolved. Considering that the baryonic mass resolution is  $\sim 10^5 M_{\odot}$ , as mentioned before, the minimum stellar mass considered is  $\geq 10^9 M_{\odot}$ .
- $f_e > 0.4$ , where  $f_e$  represents the circularity fraction, defined as the fractional mass of the stellar particles with circularity  $\epsilon > 0.7$ . The latter has previously shown to reliably select orbits confined to a disc (Aumer et al. 2013).  $f_e$  kinematically quantifies the disc's shape, thus ensuring that the galaxies selected are considered "discy" (Joshi et al. 2020).
- $R_{90} \geq 3\text{kpc}$ . This ensures that the structure of the galactic disc is clearly resolved.

These criteria result in a sample of 7,919 late-type galaxies. In Table 1 we list the parameters measured from each galaxy that are later used to train our classification models. These parameter are computed as described in Dolfi et al. (2023), and

references there in. Note that all selected parameters characterize galaxies internal properties and do not explicitly account for the environment in which the galaxies are located. Moreover, previous works have shown that some of these parameters, such as the disc central stellar density,  $\mu_*$ , and its extension,  $R_{\text{ext}}$  are expected to be strongly linked to the occurrence of lopsided perturbations. In Fig. 1 we quantify the Pearson Correlation Coefficient between the listed parameters. Checking the parameters' correlation is an important first step to ensure an accurate representation of the classifier's results, as having highly correlated data (Pearson correlation values of 1 and -1) can lead to a misinterpretation of the importance of some parameters. In our case, we note that our parameters do not show a strong correlation, with the exception of  $R_{50}$  and  $R_{\text{ext}}$ , which have a score of 0.88. This suggests that there is no issue in applying all the selected parameters in our classifier.

## 3. Methods

In this work we make use of Random Forests (hereafter RF; Breiman 2001) and its variations to study our selected dataset. Since we deal with a supervised algorithm, it is necessary to count with a training and testing set where galaxies are already labeled as lopsided or symmetric galaxies. A Fourier Decomposition of the light/mass distribution is often used to quantify asymmetries (Zaritsky & Rix 1997; Reichard et al. 2008; Varela-Lavin et al. 2023; Dolfi et al. 2023). We will use the radial distribution of the  $m = 1$  mode to label our dataset. To prepare our data before applying it to the models, we partition the dataset into a training set and a testing set comprising 70% and 30% of the

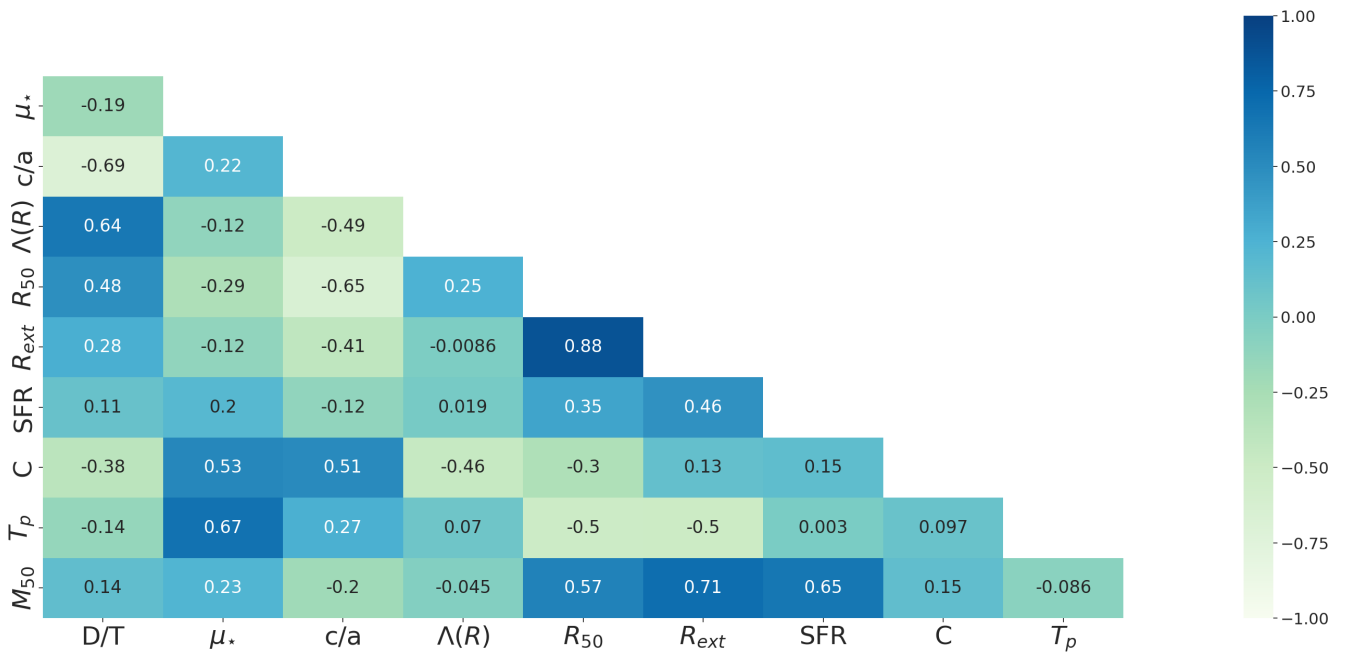


**Fig. 1.** Heatmap of the Pearson Coefficient Correlation of the features listed in Table 1.

total sample, respectively. To do so, we employ SCIKIT-LEARN<sup>1</sup>'s STRATIFIEDSHUFFLESPLIT.

In this section we first discuss how lopsidedness is measured in our models, and then introduce and summarize the main characteristics of RFs and its variations. We also discuss our particular application and the metrics used to measure its performance.

### 3.1. Measuring Lopsidedness

To label the galaxies in our sample between lopsided and symmetric, we apply a Fourier Decomposition. To do so, we measure the amplitude of the first mode  $m = 1$  of the stellar disc density distribution,  $A_1$ , which quantifies the asymmetry of the stellar mass distribution. Before doing so, we have taken into account a few considerations. First, it is crucial to ensure that each galaxy is projected face-on, as the Fourier Decomposition is highly sensitive to the disc inclination. To do so, we rotate each galaxy such as the z-axis is aligned with the disc angular momentum vector. Secondly, to focus our analysis on stellar discs, we consider only stellar particles located within a cylinder of width equal to  $1.4R_{90}$ , and a height equal to  $2h_{90}$ . Here,  $h_{90}$  is defined as the vertical distance above and below the disc plane enclosing 90% of the total galaxy stellar mass. The adopted definition for the disc extent allow us to reach their outer regions without introducing contamination from the stellar halo. We have tested several definitions for the disc extent, and found that the, overall, results are not significantly affected by our definition.

The Fourier decomposition for the stellar mass distribution is calculated as follows:

$$C_m(R_j, t) = \sum_i M_i e^{-im\phi_i}$$

where  $M_i$  and  $\phi_i$  are the mass and the azimuthal coordinate of the  $i$ -th stellar particle. The  $A_1$  radial profile is then calculated as follows:

$$A_1(R_j, t) = \frac{B_1(R_j, t)}{B_0(R_j, t)}$$

where  $B_1(R_j, t)$  and  $B_0(R_j, t)$  are the amplitude or strength of the  $m = 1$  and  $m = 0$  mode, respectively, within a certain radius  $R_j$  and a certain snapshot  $t$ . In general, the amplitude of the Fourier decomposition is given by:

$$B_m(R_j, t) = \sqrt{a_m^2(R_j, t) + b_m^2(R_j, t)},$$

where  $a_m(R_j, t)$  and  $b_m(R_j, t)$  are defined as the real and imaginary values of  $C_m(R_j, t)$  for the  $m$ -th mode, respectively.

The averaged value of  $A_1(R, t)$  at a given time,  $t$ , over a certain radial interval (hereafter  $A_1$ ) is then used as the global or large-scale lopsidedness indicator. In general, if  $A_1 > 0.1$ , the galaxy is considered lopsided. For values of  $A_1 < 0.1$  galaxies are considered symmetric. This threshold has been widely adopted in the literature, where both large observational and simulated galaxies were considered (e.g. Jog & Combes 2009; Reichard et al. 2008; Varela-Lavin et al. 2023; Dolfi et al. 2023). The radial interval considered to calculate the global  $A_1$  parameter has varied between different works. For instance, Zaritsky & Rix (1997) studied the lopsidedness distribution of a sample of 60 field spiral galaxies, using the radial interval of  $(1.5 - 2.5)$  disc scale lengths. On the other hand, Reichard et al. (2008) measured the lopsidedness of a sample obtained from SDSS in the radial interval  $R_{50}-R_{90}$ . van Eymeren et al. (2011) reached distances up to 4 to 5 disc scale lengths to study the asymmetries of the discs' outer regions. In our case, we use  $R_{50} - 1.4R_{90}$ , as we find that this radial interval best represent the non-axisymmetry of the sample.

As an example of the classification made by  $A_1$ , Fig. 2 shows the face-on projections of the surface brightness distribution in the V-band of two clearly classified cases. Here the dashed and cyan lines indicate the lower and upper radial limits, respectively, considered to compute  $A_1$ . Considering their respective  $A_1$  values, the galaxy on the left is classified as a strong symmetric

<sup>1</sup> <https://scikit-learn.org>

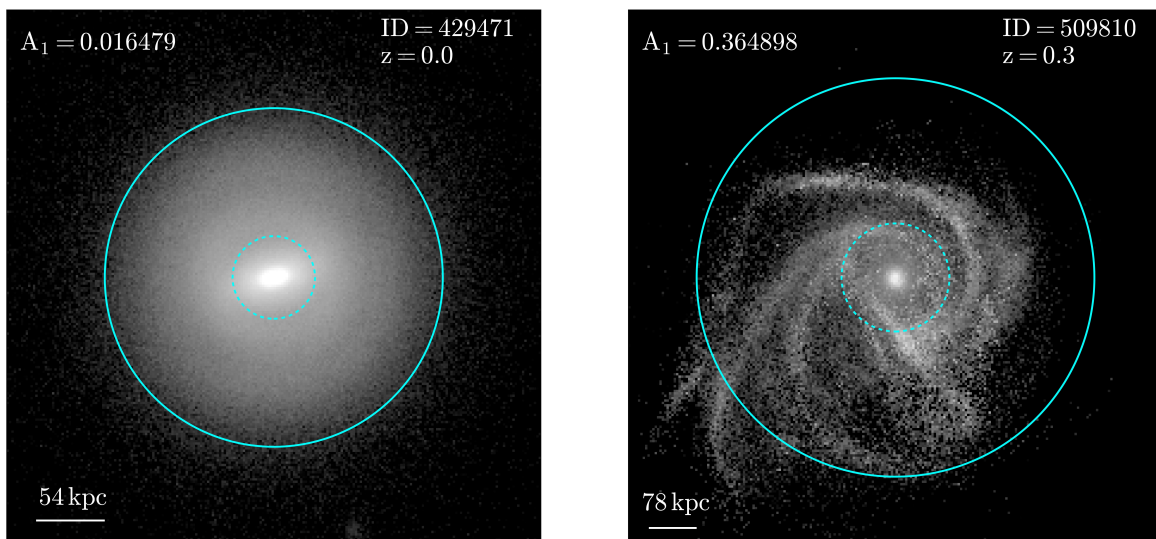


**Fig. 2.** V-band face-on projected surface brightness distribution of a symmetric (*left*) and lopsided (*right*) galaxy, considered as examples of the classification made by  $A_1$ . Their respective  $A_1$  value, ID (as in TNG50-1), and redshift snapshot are plotted on the upper side. On the lower left, the box size considered for each galaxy is also plotted. For both images, the dashed cyan line represents the radius  $R_{50}$  and the solid cyan line represents the radius  $1.4R_{90}$ , which are the limits of the radial interval used in the Fourier decomposition.

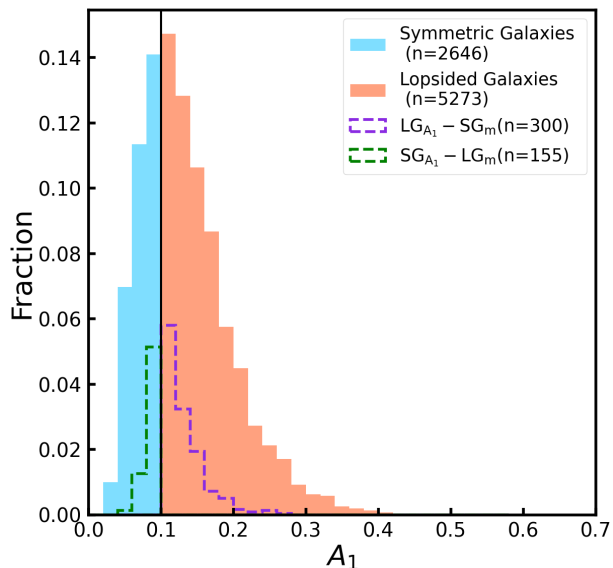


**Fig. 3.**  $A_1$  distribution of our total sample.  $A_1$  is defined as the averaged strength of the  $m = 1$  mode of the Fourier Decomposition for each stellar particle within the radial range  $R_{50} - 1.4R_{90}$ . The black line represents the threshold used to distinguish between lopsided (orange) and symmetric galaxies (blue). The dashed distributions represent the incorrect classifications of the galaxies made by SMOTE+RF for testing set, as we discuss later in Sect. 4. The purple dashed distribution represents the actual symmetric galaxies classified by the model as lopsided galaxies ( $SG_{A_1} - LG_m$ ), and the green dashed distribution represents the actual lopsided galaxies classified by the model as symmetric galaxies ( $LG_{A_1} - SG_m$ ). Each distribution has in parenthesis their respective number.

example with  $A_1 = 0.02$ , while the galaxy on the right is classified as a strong lopsided example with a value of  $A_1 = 0.36$ .

The resulting  $A_1$  distribution of our sample is shown in Fig. 3. The light blue and orange shaded areas indicate the distribution for symmetric and lopsided classified galaxies, based on the selected  $A_1$  threshold (black line). Notably, our sample is imbal-

anced; i.e. we have a higher quantity of lopsided galaxies with respect to the symmetric cases. Out of the total sample size of 7,919 galaxies, 5,273 (i.e. 65%) are classified as lopsided, while 2,646 (i.e. 35%) as symmetric. We note that we find a larger fraction of lopsided galaxies than observations in the local Universe (i.e. 30%; Zaritsky & Rix 1997; Reichard et al. 2008). As previously discussed in Dolfi et al. (2023), this difference can be likely attributed to the different radial interval used to measure the global lopsidedness  $A_1$ . For this reason, we are finding a larger fraction of lopsided galaxies than observations, due to the fact that we are reaching out to larger galactocentric radii where the lopsided amplitude is stronger (see also Varela-Lavin et al. 2023). The resulting imbalance imposes a great challenge for the training and testing of our selected machine learning algorithms. In the following section, we dive deeper into this issue and describe the methods we use to address it.

Lastly, Fig. 4 shows the distribution of our selected parameters, subdividing both types of galaxies to stress their differences. The dashed lines indicate the median of the corresponding distributions. The first and second top panels show the distributions of  $\mu_*$  and  $T_p$ . It is evident that the two galaxy types show the largest differences in these two parameters. As expected, lopsided galaxies typically show significantly smaller  $\mu_*$  than their symmetric counterparts. Similarly, lopsided galaxies exhibit smaller values of  $T_p$ . This trends are in agreement with previous results (Reichard et al. 2008; Zaritsky et al. 2013; Varela-Lavin et al. 2023) that highlighted that both types of galaxies are indeed characterized by different internal structures.

### 3.2. Classification Algorithms

RF is a type of supervised algorithm that poses a great advantage in the automation of different classification and regression tasks. For instance, it can describe different complexity relations between the parameters, or features, of a sample considering their assigned label. It can also works with a wide variety of different datasets and sizes, among other advantages. In the case of astronomy, it is clear that the use of machine learning algorithms,

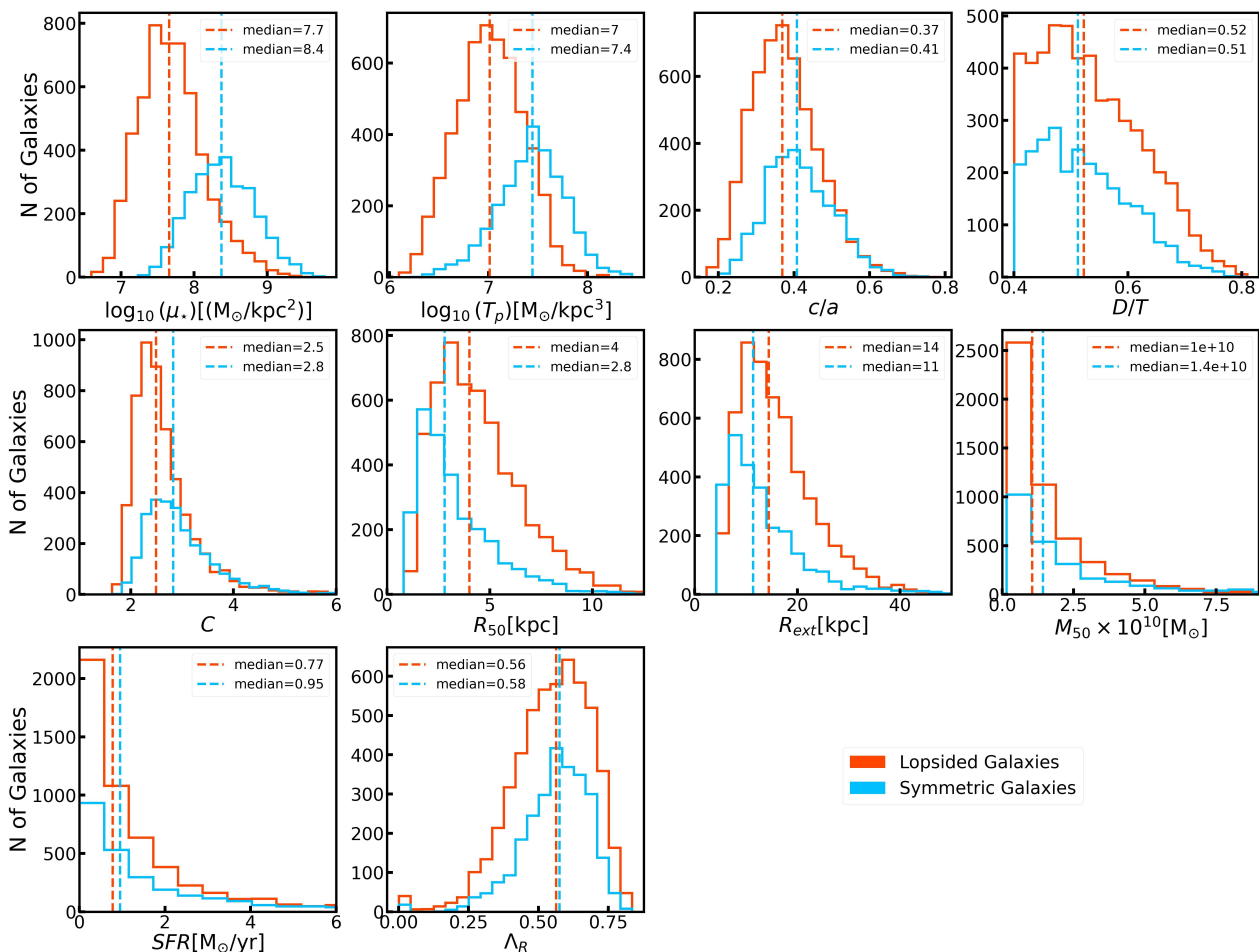


**Fig. 4.** Distribution of parameters selected to characterize our galaxy sample. These parameters are used as features by the Random Forest classifier. The orange and blue distributions represent lopsided and symmetric galaxies, respectively. The colored dashed lines represent their respective median.

such as RF, have grown as a result of the exponential increase of data with the current and next-generation surveys and telescopes. As application examples, RF poses a great alternative to classify different sources in different wavelengths (Gao et al. 2009), estimation of photometric redshifts (Carliles et al. 2010), perform automatic classification of light curves of variable stars (Sánchez-Sáez et al. 2021), predict underlying gas conditions of the circumgalactic medium (Appleby et al. 2023), identify galaxy mergers (Guzmán-Ortega et al. 2023) and estimate different galaxies' physical properties (Mucesh et al. 2021), among other applications.

RF consists of an ensemble, or collection, of decision trees. A decision tree is a tree-like predictive model composed of nodes, where the sample is recursively divided by conditions in the form of  $x_i^{(j)} < X_j$ , the latter being the  $j$ -th feature and  $x_i^{(j)}$  a certain threshold based on the  $j$ -th feature. In other words, decision trees divide the input space, which depends on the selected feature/s by the decision tree, to create subspaces that are able to differentiate between the different classes. The quality of this division is measured by the "purity" of the subspace, where the purer it is, the more datapoints from the same class are assigned. The final nodes, called leaves or terminal nodes, result by either fully partitioning the sample or until all leaves have less than the minimum quantity to split a node, which is determined by a certain parameter in the tuning process, discussed below. For classification tasks, these final nodes provide predictions of a certain

class based on the resulting probability or, in the case of regression tasks, they provide a numeric value. This process is done firstly on a learning set, or training set, where then a new unseen dataset is propagated over the tree to predict the corresponding class or numeric value.

Although decision trees have numerous advantages due to their intrinsic nature (e.g., they can be used by any kind of sample, they have an easy hyperparameter customization or tuning, and they also estimate the feature importance aside from class predictions), they are easy to overfit. This means that a decision tree may be less accurate when predicting unseen data during testing, as the model tends to overly fit to the training set. RF avoids this issue by training non-correlated decision trees, each on a subsample with replacement of the training set, thus reducing the variance while maintaining high accuracy. For a binary classification task, which is our focus, each decision tree classifies the data as either positive or negative class. Then, the final prediction of the RF is the class predicted by more than half of the trees. This method is called bagging or *bootstrap aggregating* (Breiman 1996).

Due to our dataset being imbalanced, as seen in Fig. 3, using a RF classifier could lead to an inaccurate classification. The training and testing of the RF are performed considering bootstrapped samples of the corresponding data sets. As each sample follows the same distribution as the original dataset, the majority class would have more predictions in favor, thus having more



**Table 2.** Results of the hyperparameter tuning using RANDOMIZED-SEARCHCV for each model.

Hyperparameters	SMOTE+RF	BRF
number of trees	1500	128
minimum samples split	5	5
minimum sample leaf	2	2
maximum features	sqrt	log2
maximum depth	75	200
sampling strategy	-	all

accurate results than the minority class. To avoid this issue affecting our results, we employ two different algorithms. The first one consists on oversampling the minority class of the training set and then apply it to a RF classifier. To do the oversampling, we use IMBALANCED-LEARN<sup>2</sup>'s SMOTE (Bowyer et al. 2011) method. This creates new "synthetic" data by interpolation between two close datapoints in the multidimensional feature space; in our a 10 dimensional feature space. The second algorithm consists of using Balanced Random Forests (hereafter BRF; Chen & Breiman 2004)), where we use IMBALANCED-LEARN'S BALANCED-RANDOMFORESTCLASSIFIER method. In this case, the bootstrapped sample is only considered for the minority class, whereas the majority class is randomly sampled with replacement, matching the size of the minority class. This avoids manually oversampling the dataset and it is directly performed by each decision tree.

To have an optimal performance of both classifiers using our datasets, we perform an *hyperparameter tuning*, which involves finding the best combination of parameters from the models to yield the best results. The parameters involved in the fitting of the RF classifiers are listed in Table 2 with their respective results. To tune both models, we use RANDOMIZEDSEARCHCV with number of iterations  $n_{iter} = 10$  and, as cross-validation, REPEATEDSTRATIFIEDKFOLD with number of repeats  $n_{repeat} = 10$  and number of splits  $n_{splits} = 5$ . In both cases, the  $n_{iter}$ ,  $n_{repeat}$ , and  $n_{splits}$  are the default values of the parameters. To avoid unnecessary complexity in the calculations, we retain the default values for the current and following analysis. For the tuning process, we select a range of possible values for each hyperparameter and then apply it to the randomized search. This generates random combinations of hyperparameters and selects the combination that yields the best performance based on a chosen metric, which in our case is balanced accuracy. It is worth highlighting the significant difference in the number of trees between both classifiers, where SMOTE+RF has 1,500 trees in comparison with BRF, which has 128. This discrepancy in the number of trees might be attributed to the added complexity and variability introduced to the minority class by the SMOTE oversampling process. As it creates synthetic data, the complexity and variability of the sample increases, requiring SMOTE+RF to utilize a larger ensemble of trees to effectively generalize the data and achieve robust results.

### 3.3. Evaluation Metrics

To measure the performance of both SMOTE+RF and BRF, we use the following metrics considering the use of binary classifiers:

- Precision: Ratio of the number of correctly predicted positive class to the total number of predicted positive class. Expressed as:

$$\text{Precision} = \frac{TP}{FP + TP}$$

- TPR: Ratio of the number of correctly predicted positive class to the number of actual positive class. Expressed as:

$$\text{TPR} = \frac{TP}{FN + TP}$$

- F1-score: Harmonic mean of precision and TPR. Expressed as:

$$\text{F1 - score} = 2 \times \frac{\text{precision} \times \text{TPR}}{\text{precision} + \text{TPR}}$$

- True Negative Rate (TNR) or specificity: Ratio of the correctly predicted negative class to the total number of the actual negative class. Expressed as:

$$\text{TNR} = \frac{TN}{FP + TN}$$

- Balanced Accuracy: Average of the recall obtained for each class Expressed as:

$$\text{balanced accuracy} = \frac{1}{2} (\text{TNR} \times \text{TPR})$$

- Geometric Mean (*G-mean*): Square root of TNR and TPR. Expressed as:

$$\text{G - mean} = (\text{TNR} \times \text{TPR})^{1/2}$$

- ROC-AUC: Calculates the area under the Receiver Operating Characteristic (ROC) curve, by using the trapezoidal rule, which approximates the area under the curve as a series of trapezoids. Considering a series of points in the ROC curve, in the form of  $(x_1, y_1), (x_2, y_2), \dots, (x_N, y_N)$ , the area under the curve is expressed as:

$$\text{ROC - AUC} = \sum_{i=1}^{N-1} \frac{(x_{i+1} - x_i)(y_i + y_{i+1})}{2}$$

The selected metrics are used to evaluate the results of our classifiers. In particular, precision, TPR, and F1-score are important metrics to evaluate the performance of any type of model. However, these metrics are all sensitive to imbalanced dataset. As a result, they could mislead the algorithm during the training and validation process. To avoid this, we focus the analysis of our classifiers to TNR, balanced accuracy, and G-mean. This metrics are selected following Cheng et al. (2020) work, which ensure a correct analysis due to the imbalanced nature of our dataset. Lastly, we also consider ROC-AUC for the analysis, as it gives us an important insight on how the model is performing without any effect of the imbalance. Still, we present the values for TPR, precision, and F-score, as a reference.

<sup>2</sup> <https://imbalanced-learn.org>

**Table 3.** Metric scores of the selected model, SMOTE+RF, applied to the testing set. Each score is obtained by averaging the iterations of a cross-validation with  $n_{iter} = 5$  and taking into consideration its standard deviation.

Metric	SMOTE+RF	BRF
	Score	Score
Precision	0.702±0.013	0.675±0.007
TPR	0.797±0.019	0.833±0.014
F1-score	0.746±0.012	0.746±0.007
ROC-AUC	0.813±0.010	0.816±0.006
TNR	0.830±0.011	0.799±0.00
G-mean	0.813±0.010	0.816±0.006
Balanced-Accuracy	0.813±0.010	0.816±0.006

## 4. Results & Analysis

### 4.1. Classification results

In this section, we introduce and analyze the results of the algorithms for the automatic classification between lopsided and symmetric galaxies. As a brief outline of our classification pipeline, we train the classifiers mentioned in Sect. 3.2 with 5,542 galaxies, constituting 70% of the total sample. This enables the algorithm to obtain important underlying patterns and/or relationships between the galaxies and their features, which are then used for the prediction in the final step. The remaining galaxies are considered for the testing set, which comprises a total of 2,377 galaxies, or 30% of the remaining sample. For each galaxy, these decision trees produce a class prediction—either lopsided or symmetric—and the class that is predicted in more than half of the decision trees is taken as the final prediction for that galaxy. Due to the imbalanced nature of our dataset, we define lopsided as the negative class and symmetric galaxies as the positive class. Usually, the majority class is better represented and naturally favorable by the algorithm over the minority class. To avoid this problem, we designate the minority class as the positive class, which helps with the interpretability of metrics, such as TPR, precision, and ROC-AUC for rare cases. Since we also obtain a proxy of the probability of a galaxy being in the positive/negative class, we test different thresholds, or *cut-off*, to classify the samples and to explore how such threshold can affect our results. As a default, this threshold is set at 0.5, i.e. galaxies with probabilities equal or greater than this value are labeled as the positive class or, in our case, symmetric galaxies. Galaxies with probabilities lesser than this value are labeled as the negative class; i.e. lopsided galaxies. Our analysis showed that differences in the results obtained between the different *cut-offs* is negligible. Therefore the following analysis was performed with the default value, 0.5, for SMOTE+RF and BRF.

The results of each model’s performance for the testing set are listed in Table 3. Each value of the metrics is obtained by averaging the result scores of each iteration of a cross-validation with number of iterations  $n_{iter} = 10$ , which is the default value, and taking into consideration its standard deviation. It is clear that both classifiers provide similar results, with comparable values in most metrics. Based on this, we select as our classifier SMOTE+RF since it results in better TNR metric. As previously discussed, we are working with a unbalanced data set, with more than 70% of the data belonging to the negative class (lopsided objects). Thus, a high TNR indicates a better performance for the most populated class of our sample.

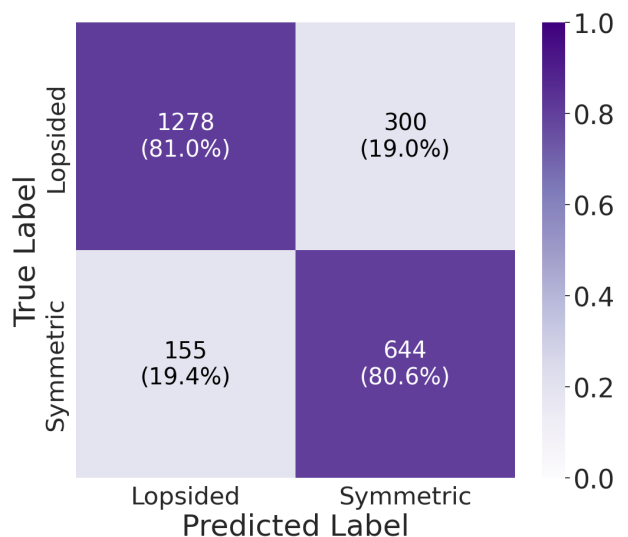


**Fig. 5.** Confusion matrix for the testing set of the best model, SMOTE+RF. The x-axis is the predicted class or predicted label, and the y-axis is the actual class or actual label. The percentage with respect each type of galaxy set is on parenthesis.

Fig. 5 shows the confusion matrix (CM) for SMOTE+RF. The x-axis indicates the predicted class or predicted label, obtained from the classifier, and the y-axis show the actual class or actual label, obtained from the  $A_1$  parameter. In general, a CM allows us to visually inspect the fractions of correct and incorrect classification we have obtained. In our testing sample, and based on our  $A_1$  classification criteria, we count with 1,578 true lopsided and a total 799 true symmetric galaxies. Interestingly our classifier is able to correctly classify 81% of the lopsided object and approximately the same amount for their symmetric counterparts. In absolute number, we obtain a total of 1,922 correctly classified galaxies, against 455 wrongly classified objects. It is worth highlighting the very good performance of the SMOTE+RF classifier, which has been purely obtained based on features that are related to our simulated galaxies internal properties. No information about environments has been introduced during the training process.

### 4.2. Interpretation of the Random Forest classification

Supervised algorithms, including RFs, suffer from interpretability of the decisions leading to the classification. This is often called the "black box" problem. In RFs, it arises due to the high quantity of decision trees added to the ensemble. In this section, we interpret and analyze the decisions lead by the model to subdivide the galaxies between lopsided and symmetric by ranking the importance of the features used in the classification process.

We use the *permutation\_importance\_* attribute from `RANDOMFORESTCLASSIFIER`. There are various methods for ranking feature importance, but given the continuous nature of our dataset—where no categorical features are used for training or testing— we rely solely on *permutation\_importance\_*. This attribute works by permuting, or shuffling, the values of each feature and calculating the resulting decrease of a specified metric, which by default is accuracy, defined as the fraction or count of the correct predictions. The decrease in the score is then used to rank each feature: the higher the score, the more it affects the model’s performance, thus making the feature important for the model to maintain a higher accuracy. However, since our dataset



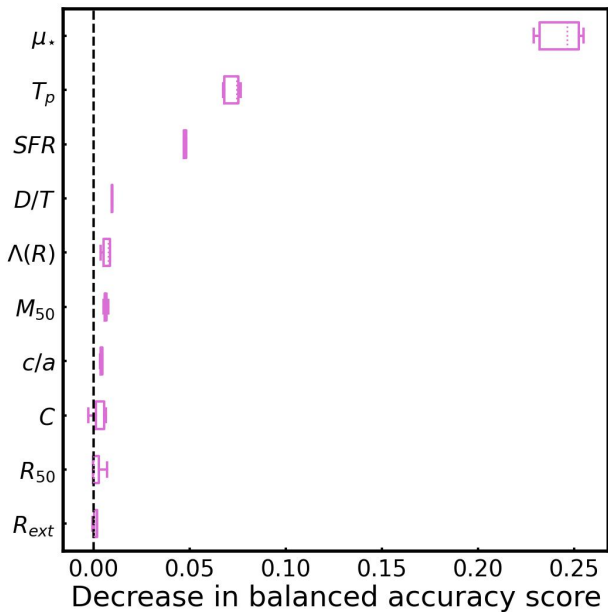


**Fig. 6.** Box plot of each feature from the testing set, ranked by their importance as determined by the *feature\_permutation\_* attribute from SMOTE+RF. Each box represents the range of the different scores obtained from a cross-validation with  $n_{iter} = 5$ . The inner dashed line represents the median value of each distribution. The whiskers on each box represent the minimum and maximum value of each distribution.

is imbalanced, using accuracy would not return an accurate representation of the importance of our features. To address this issue, we use balanced-accuracy instead. As discussed in Sec. 3.3, this metric represents the averaged fraction of correct classified galaxies for both the negative and positive class. In this, each class contribute equally to the final score, regardless of its size. Considering that the accuracy metric disproportionately favors the majority class in imbalanced datasets due to its overrepresentation, balanced accuracy is great a alternative to avoid inaccurate results.

The results of this procedure are shown in Table 4, where lists the rank of each feature obtained by *permutation\_importance\_*. Considering that we want to focus on the performance of SMOTE+RF with unseen data, we only calculate the feature importance for the testing set. We obtain each score by averaging the iterations of a cross-validation with  $n_{iter} = 5$  and taking into consideration its standard deviation. This analysis clearly sows that both  $\mu_*$  and  $T_p$  are the highest-ranked parameters, with  $\mu_*$  ranked first  $T_p$  ranked second. As a way to better visualize this, Fig. 6 also shows the variation of balanced-accuracy with a box plot. Each box represents the distribution of the score value for each iteration. The dotted line inside each box is the median of the distribution, and each whisker represents the first and last score value. Indeed, we note that  $\mu_*$  is the top-ranked parameter overall, indicating that it is the most important parameter to consider in the classification process made by SMOTE+RF. As we previously mentioned, and as seen in Fig. 4, lopsided and symmetric galaxies are characterized by different  $\mu_*$  distributions. This is in agreement with previous results (Reichard et al. 2008; Zaritsky et al. 2013; Varela-Lavin et al. 2023; Dolfi et al. 2023), where lopsided galaxies tend to show significantly lower a densities in the inner regions (as defined by their  $R_{50}$ ) with respect to the symmetric counterparts.

Although not as important as  $\mu_*$ ,  $T_p$  and  $SFR$  also play an important role in the classification process in comparison with

**Table 4.** Feature Importance of each parameter calculated by *permutation\_importance\_* for SMOTE+RF. The score is obtained averaging each iteration of a cross-validation with  $n_{iter} = 5$ , which is the default value, and taking into consideration its standard deviation.

Rank	Feature	Score
1	$\mu_*$	0.242930±0.010621
2	$T_p$	0.072285±0.003824
3	$SFR$	0.047444±0.005302
4	$DT$	0.009005±0.002047
5	$\Lambda(R)$	0.006586±0.002012
6	$M_{50}$	0.006234±0.000864
7	$c/a$	0.004205±0.000934
8	$C$	0.003042±0.003434
9	$R_{50}$	0.001760±0.002815
10	$R_{ext}$	0.000721±0.000990

the rest of the features. This is also in agreement with previous results, where an (anti-) correlation between lopsidedness and  $T_p$  (e.g. Gómez et al. 2016) and a correlation between lopsidedness and  $SFR$  (e.g. Conselice et al. 2000) have been reported. In particular,  $T_p$  represents a proxy of the tidal force exerted by the inner galactic regions on the outer disk material. In other words, it indicates how gravitationally cohesive a galaxy is. The relevance of this parameter is clearly reflected in the separation between the distribution of both types of galaxies, as previously seen in Fig. 4, where lopsided galaxies tend to have lower values of  $T_p$  than symmetric galaxies. These findings align with the conclusions of Varela-Lavin et al. (2023) and Dolfi et al. (2023), which propose that lopsided perturbations serve as indicators of intrinsic galaxy properties, rather than being predominantly driven by environmental processes. In other words, galaxies with low central stellar densities are weakly gravitationally cohesive and, thus, are more susceptible to lopsided perturbations, independently of the particular perturbing agent. On the other hand,  $SFR$  ranking third place is an interesting result, as it is been shown that there is a correlation between  $A_1$  and current  $SFR$  (Zaritsky & Rix 1997; Rudnick et al. 2000; Reichard et al. 2009). As discussed by Łokas (2022), some internal properties of lopsided and symmetric galaxies can be linked with their current  $SFR$ , e.g. lopsided galaxies having bluer colors, larger gas fractions, and lower metallicity than symmetric galaxies. Moreover, Dolfi et al. (2023) showed that lopsided galaxies tend to be, on average, significantly more star forming than symmetric galaxies at later times. Symmetric galaxies, on the contrary, have an earlier assembly with shorter and more intense star forming bursts. As a result, and considering galaxies with similar stellar masses at the present-day, while symmetric galaxies tend to develop a more pronounce central region at earlier times, lopsided galaxies tend to form at larger fraction of their stellar populations later, typically developing a more extended stellar disc and less dense inner regions. Lastly, Fig. 6 shows the relative importance of the remaining 7 features. It is clear that they have a minimal impact on the classification procedure.

To analyze the classification made by SMOTE+RF, we plot in Fig. 7 the median of  $A_1$  as a function of radius for the four cases defined by the classifier. To generate this figure, the radial extension of each simulated galaxy was normalized by its corresponding  $R_{90}$ . We focus on the radial interval  $(0.5 - 1.4)R_{90}$ , as it is the considered interval for the Fourier decomposition. The shaded areas represent the 25th and 75th percentiles of the distribution. In the left plot, the fuchsia distribution represents correctly classified lopsided galaxies ( $LG_{A_1} - LG_m$ ) whereas the

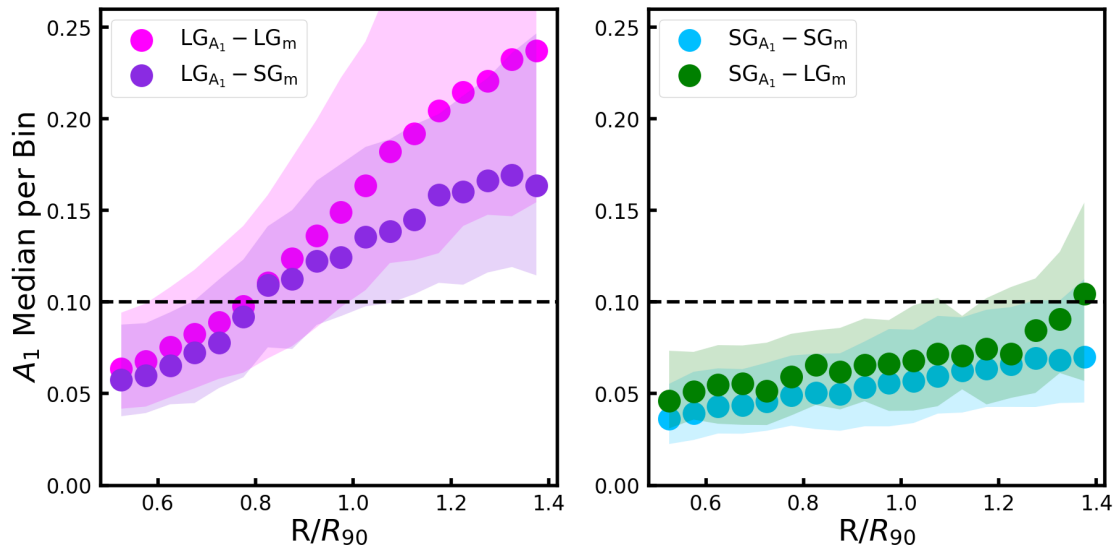


**Fig. 7.** Radial profiles of  $A_1$  for our four classification cases, calculated as the median of  $A_1$  for each bin with respect to  $R_{90}$ . The fuchsia and blue distributions represent the correctly classified lopsided galaxies ( $LG_{A_1} - LG_m$ ) and symmetric galaxies ( $SG_{A_1} - SG_m$ ), respectively. The green distribution represents symmetric galaxies classified as lopsided ( $SG_{A_1} - LG_m$ ) and the purple distribution represents lopsided galaxies classified as symmetric ( $LG_{A_1} - SG_m$ ). The shaded areas represent the 25th and 75th percentiles of each sample.

purple distribution represent lopsided galaxies classified by our model as symmetric ( $LG_{A_1} - SG_m$ ). The right plot is the same as the left one but for symmetric galaxies. Here the cyan color represent the distribution of correctly classified symmetric galaxies, ( $SG_{A_1} - SG_m$ ), while in green we show symmetric galaxies classified as lopsided ( $SG_{A_1} - LG_m$ ). Note that incorrectly classified cases do not follow the same trend as the correctly classified distributions. In the case of ( $LG_{A_1} - SG_m$ ) on the left plot, from  $0.5R_{90}$  to  $0.9R_{90}$  the magnitude of  $A_1$  starts increasing at the same rate than the correctly classified sample. However, from  $0.9R_{90}$  onward, the slope is less steep, meaning that the magnitude of  $A_1$  does not increase as much as in ( $LG_{A_1} - LG_m$ ). In other words, while incorrectly classified galaxies have indeed an outer perturbed region, the strength of the perturbations is typically weaker with respect to correctly classified galaxies. On the right panel we show that the  $A_1$  profile of both correctly ( $SG_{A_1} - SG_m$ ) and incorrectly classified galaxies ( $SG_{A_1} - LG_m$ ) remains below the 0.1 threshold chosen to classify lopsided galaxies based on the  $A_1$  parameter. Nonetheless, wrongly classified symmetric galaxies tend to have a larger  $A_1$  value at all radii and they do cross the threshold at the outermost edge. In the following section we explore in detail the main reasons that drove the SMOTE+RF method to misclassify these galaxies.

### 4.3. Interpretation of the Misclassified Cases

In the previous section, we analyzed the results of applying RFs algorithms to the internal parameters of our selected sample of lopsided and symmetric galaxies. In particular, we find that the  $\mu_*$  and  $T_P$  parameters are the primary features used by the classifier to subdivide galaxies as either lopsided or symmetric, consistent with previous observational studies. However, there are 455 galaxies in the testing set that are misclassified. In this section, we focus on the misclassified cases, ( $LG_{A_1} - SG_m$ ) and ( $SG_{A_1} - LG_m$ ), to investigate the underlying reasons behind the misclassification.

To further study the incorrectly classified galaxies, in Figure 3 we highlight their  $A_1$  distributions. The purple dashed distribution represents lopsided galaxies classified as symmetric galax-

ies ( $LG_{A_1} - SG_m$ ) with a median of  $\sim 0.09$ , and the green dashed distribution represents symmetric galaxies classified as lopsided galaxies ( $SG_{A_1} - LG_m$ ) with a median of  $\sim 0.12$ . It is clear that all misclassified galaxies are adjacent to the threshold  $A_1 = 0.1$  and, thus, represent challenging cases for our classification models. In Fig. 8 we show the distribution of  $\mu_*$ ,  $T_P$ , and  $R_{90}$  for all the four different classification cases, following the same color coding as in Fig. 7. Each dashed line represents the median of the corresponding distribution. The top panels show the results obtained from the correctly classified galaxy samples by our model. Note that the distributions differ significantly in all three parameters. As expected, the largest differences are found in  $\mu_*$ . However, even the  $R_{90}$  distributions differ, with median values of 11 kpc and 14.3 kpc for symmetric and lopsided galaxies, respectively. The bottom panels show the distributions obtained from the incorrectly classified samples. Two important things stand out. First, the distributions of the three inspected parameters show more significant overlap with respect to the correctly classified sample. The medians are, in all cases, closer to the median of the overall sample. This is most clear in the  $R_{90}$  distributions, where both symmetric and lopsided nearly perfectly overlap with each other. Second, and most importantly, we find that galaxies classified as lopsided by our global  $A_1$  parameter, but identified as symmetric by our model ( $LG_{A_1} - SG_m$ ), have values of  $\mu_*$  and  $T_P$  that are consistent with the distribution of correctly classified symmetric galaxies. In other words, they have relatively large central surface density and  $T_P$  values. Upon closer inspection of their images, we observe that such galaxies typically display a symmetric overall disk, but a significant asymmetry in their outermost region. An example of such galaxy is show in the top right panel of Figure 9. These localized asymmetries, captured by the global  $A_1$  parameter, not necessarily reflect the overall structure of the disc and can be caused by recent episodes of gas accretion or very recent strong interactions. On the other hand, galaxies classified as symmetric by the global  $A_1$  parameter but symmetric by our model ( $SG_{A_1} - LG_m$ ) show low  $\mu_*$  and  $T_P$  values. Such galaxies display internal properties of typical lopsided galaxies, but simply the morphological perturbation has not yet

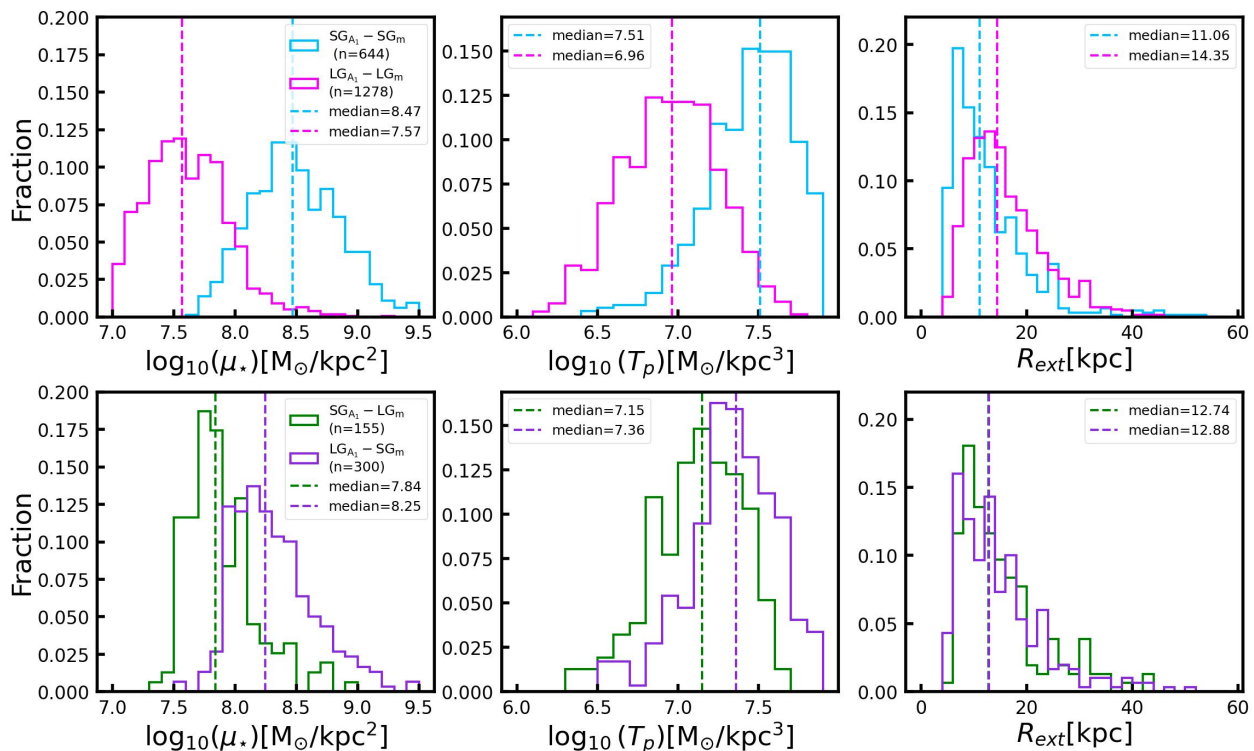


**Fig. 8.** Normalized distribution of  $\mu_*$  (left),  $T_p$  (middle), and  $R_{ext}$  (right), considering the correct (upper) and incorrect (bottom) classification made by SMOTE+RF. Each distribution has been normalized by their corresponding number of galaxies of each subsample. Their respective number of galaxies is in parenthesis. The fuchsia and blue distributions represent the correctly classified lopsided galaxies ( $LG_{A_1} - LG_m$ ) and symmetric galaxies ( $SG_{A_1} - SG_m$ ), respectively. The green distribution represents symmetric galaxies classified as lopsided ( $SG_{A_1} - LG_m$ ) and the purple distribution represents lopsided galaxies classified as symmetric ( $LG_{A_1} - SG_m$ ). The dashed lines represent the median of their respective distribution.

been triggered. The top left panel of Fig. 9 shows an example of such situation.

To further explore the two examples of misclassified galaxies, in the second and third row of Fig. 9 we show their radial  $A_1$  and density profiles, respectively. The cyan regions in the second row highlight the radial interval  $(0.5 - 1.4)R_{90}$ , considered to measure  $A_1$ . It is worth noting that both galaxies were selected by considering extreme values of  $\mu_*$  and  $T_p$  while having similar stellar mass. For ( $SG_{A_1} - LG_m$ ), the galaxy shows consistently low  $A_1(R)$ , even up to the disc outermost regions. Interestingly, its inner stellar density is notably lower than expected for a symmetric galaxy. Even its  $\mu_*$ , highlighted with a red star, falls below the mean of the overall sample (dashed magenta line). On the other hand, for the ( $LG_{A_1} - SG_m$ ), while the  $A_1(R)$  shows values consistent with 0 within most of the considered radial range, it shows a very strong rise in the disc outskirts. We note that this galaxy has a denser inner stellar region, highlighted by its large  $\mu_*$  value which significantly surpass the median of the overall distribution.

To understand these unexpected behavior, we explore on the two lower rows the time evolution of the lopsided parameter and the orbital histories. Interestingly, we find that the ( $LG_{A_1} - SG_m$ ) galaxy (right panels) became a satellite of a larger host approximately 1.5 Gyr ago. Previous to the pericentric passage, this galaxy showed  $A_1$  values below the threshold. After the close interaction, the  $A_1$  value rapidly grows as a result of the tidal perturbation of its outer disc. Indeed, we find that this galaxy has internal properties consistent with the symmetric sample, but the strong recent interaction forced an outer tidal disruption, captured by the  $A_1$  parameter. In the case of the ( $SG_{A_1} - LG_m$ ) (left

panels), the time evolution of  $A_1$  shows that, over most of its evolution, this galaxy was indeed strongly lopsided. The initial perturbations was likely induced by significant interaction with a massive satellite galaxy ( $\sim 1:10$ ) 6.5 Gyr ago (first pericentric passage). After this point, the galaxy suffered no other interaction with satellite of mass ratios  $< 1:100$ . Thus, the lopsided perturbation gradually relaxed, reaching a present-day  $A_1$  value below the considered threshold. Even though its internal structure make this galaxy susceptible to lopsided perturbations, the lack of significant external perturbation during its late evolution resulted on a symmetric configuration at the present-day.

We note that recent interactions cannot explain all the misclassified cases. Indeed, only 76 of the 300 ( $LG_{A_1} - LG_m$ ) cases are satellite galaxies of a more massive host. Eight (8) additional galaxies have suffered significant interactions ( $> 1:20$ ) as centrals during the last 3 Gyr. Thus, important interaction can be attributed to this misclassified class in only 28% of the cases. Nonetheless, as previously discussed, other mechanisms such as gas accretion, instability in a counter-rotating disc and torques from an off-centered dark matter halo could be at play in the remaining cases (Jog & Combes 2009). Among these mechanisms, asymmetric gas accretion has been proposed as a common driver of lopsidedness. As shown by Bournaud et al. (2005), interactions and mergers can trigger strong lopsidedness in some cases, but they do not account for all the observed statistical properties, such as a correlation between lopsidedness and the Hubble Type, or a correlation between  $m = 1$  and  $m = 2$  asymmetries, among others. In a follow up study we will focus on the misclassified cases to further the origin of lopsidedness in galaxies with internal properties common to symmetric discs.



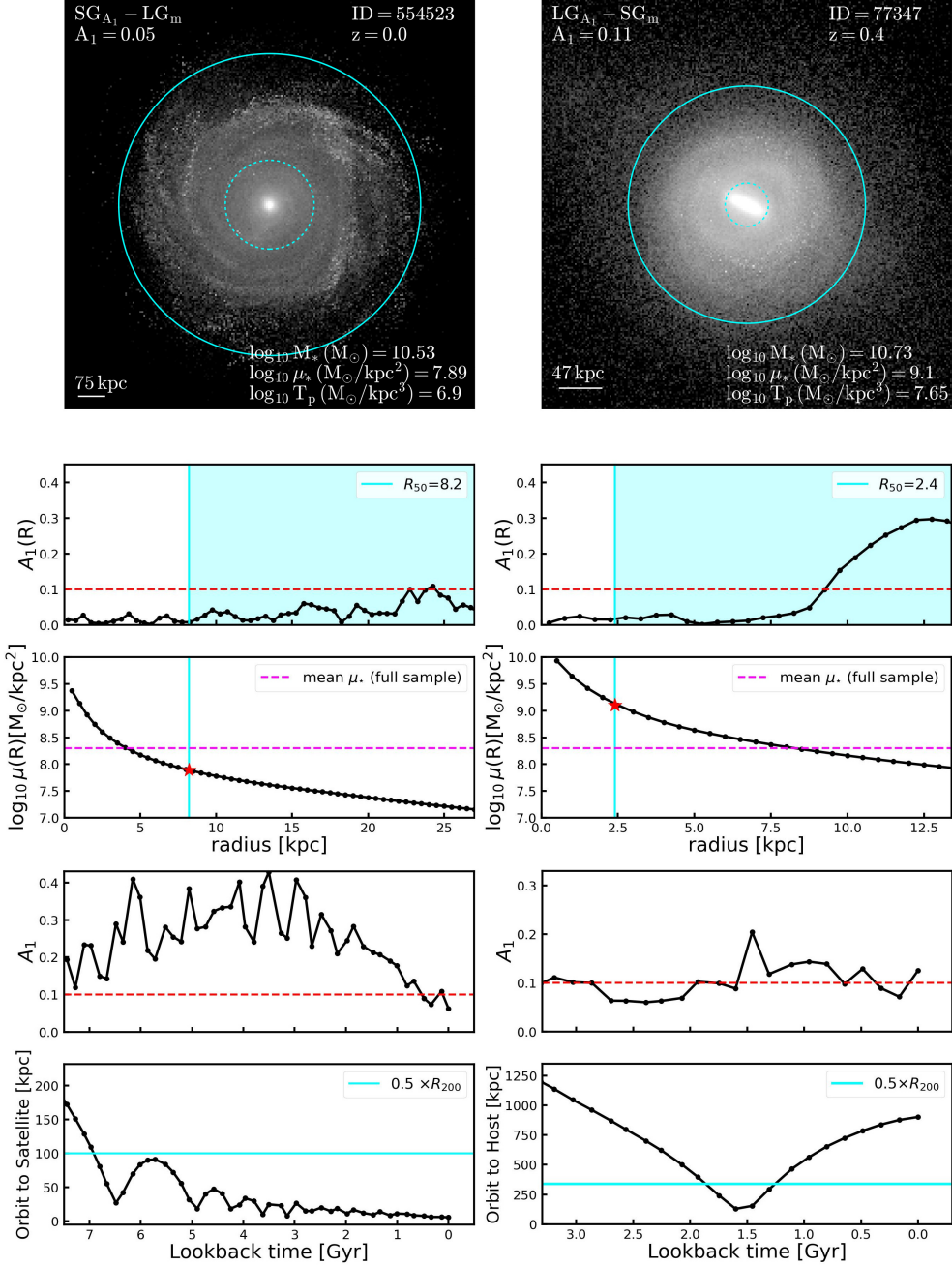


**Fig. 9.** (Top panels) V-band face-on projected surface brightness distribution of a (left) symmetric galaxy classified as lopsided ( $\text{SG}_{A_1} - \text{LG}_m$ ) and a (right) lopsided galaxy classified as symmetric ( $\text{LG}_{A_1} - \text{SG}_m$ ), considered as examples of the misclassification made by SMOTE+RF. On the upper side, their respective  $A_1$  value and classification case are plotted on the left, and their ID and redshift  $z$  on the right. On the bottom right, the values of the stellar mass ( $M_*$ ), central stellar mass density ( $\mu_*$ ), and tidal parameter ( $T_p$ ) are plotted. The dashed cyan lines represent the inner radius  $R_{50}$  and the solid cyan lines represent the outer radius  $1.4R_{90}$ , which are the limits of the radial interval used in the Fourier decomposition. (Middle panels) Lopsidedness and stellar density profiles with respect to the radius, up to  $1.4R_{90}$ . In both cases, the cyan lines represent the start of the radial interval,  $R_{50}$ . The pink dashed lines represent the average central stellar mass density ( $\mu_*$ ) of the full sample, with a value of 8.3, while the red stars represent the value of the central stellar mass density of the galaxy,  $\mu_*$ , within  $R_{50}$ . (Bottom panels) Lopsidedness and the respective orbit of the most massive satellite with respect to lookback time. The red dashed line represents the  $A_1$  threshold to classify lopsided and symmetric galaxies. The horizontal cyan line represents  $0.5 \times R_{200}$ , where  $R_{200}$  is defined as the virial radius of the central galaxy.

#### 4.4. Classification with observable parameters

Several parameters considered in this work as features require additional modeling to be estimated. Thus, they cannot be directly obtained from observation based on, e.g., photometric

data. For example, the calculation of  $\mu_*$  involves the application of additional stellar population models. Indeed, Reichard et al. (2008) calculated the stellar surface mass density following Kauffmann et al. (2003) definition, which considers the stellar mass and the Petrosian half-light radius in the z-band. Their

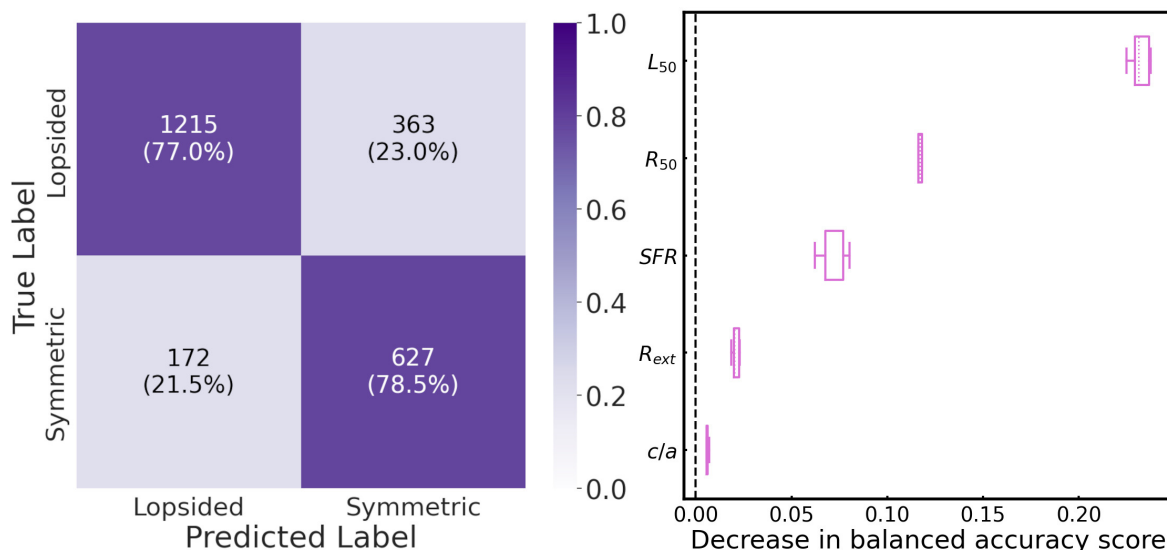


**Fig. 10.** (left) Confusion matrix of the testing set using SMOTE+RF with only observational parameters. The x-axis is the predicted class or predicted label, and the y-axis is the actual class or actual label. The percentage with respect each class is on parenthesis. (right) Box plot of each observational feature from the testing set, ranked by their importance as determined by the `feature_permutation_` attribute from SMOTE+RF. Each box represents the range of the different scores obtained from a cross-validation with  $n_{iter} = 5$ . The inner dashed line represents the median value of each distribution. The whiskers on each box represent the minimum and maximum value of each distribution.

stellar massed where estimated using a method that combines spectral diagnostics of star formation histories with photometric data. Additionally, the tidal parameter  $T_P$ , requires an estimation of the total mass enclosed within  $R_{50}$ , which involves dynamical modeling of the galaxy.

Despite their importance of in the classification process of such parameters, in this section we explore whether it is still possible to obtain a reliable classification of lopsided and symmetric galaxies using parameters that are more readily obtainable from photometric data. We follow the same pipeline mentioned earlier, but we train and test the SMOTE+RF classifier with a subset of features that could be estimated from multi-band photometric surveys such as S-Plus (Mendes de Oliveira et al. 2019) and J-Pass (Benitez et al. 2014). In particular, we replace the parameter  $M_{50}$  by the galaxies r-band luminosity within  $R_{50}$ ,  $L_{50}$ , thus avoiding the need of stellar population models. In addition to  $L_{50}$ , we consider as features  $R_{50}$ ,  $R_{ext}$ ,  $c/a$ , and  $SFR$ . The later can be obtained from narrow band photometry around the  $H_\alpha$  line through the Kennicutt relation (Kennicutt 1998). We keep the same hyperparameters listed in Table 2, along with the same training and testing sets.

The results of this test are presented in Table 5, where list the metrics obtained from the testing set. Interestingly, we find very good results, with a performance of the SMOTE+RF algorithm that is only very mildly affected by the limited number of features considered. Indeed, most scores are not significantly affected. Compared to our previous results we find a negligible decrease of 0.4% for balanced accuracy and no change for TNR. Additionally, ROC-AUC has a score of 80.9%, which reflects on how well the model is able to differentiate between both classes. As expected, substitution  $M_{50}$  by  $L_{50}$  did not introduced a significant drop in the performance. To further characterize our classification, the left panel of Fig. 10 shows the resulting CM. Note that we obtain a total of 1,927 correctly classified galaxies and only 535 incorrectly classified cases, which represent a 15% increase. Compared to our previous results, this model improves in the identification of actual lopsided galaxies, but performs slightly worse in classifying actual symmetric galaxies

**Table 5.** Scores of the SMOTE+RF model on the testing set, using only observational parameters. Each score is obtained by averaging the iterations of a cross-validation with  $n_{iter} = 5$  and taking into consideration its standard deviation.

Metric	Score
Precision	$0.691 \pm 0.012$
TPR	$0.770 \pm 0.018$
F1-score	$0.728 \pm 0.009$
ROC-AUC	$0.799 \pm 0.009$
TNR	$0.827 \pm 0.010$
G-mean	$0.798 \pm 0.009$
Balanced-Accuracy	$0.799 \pm 0.009$

as symmetric. The feature importance ranking is shown on the right panel of Fig. 10, generated with the `feature_importance` attribute. We find that the most important parameters are now  $L_{50}$ ,  $R_{50}$  and  $SFR$ . As before,  $c/a$  provides no significant information for the RF classifier.

Our results show that using readily available observational parameters offers a simpler and reliable approach to classify lopsidedness in large observational samples of galaxies, without the need of parameters that required additional modeling to be estimated, such as  $\mu_*$  and  $T_P$ . This approach could be particularly valuable in large-scale surveys such as those soon will be provided by LSST (Ivezić et al. 2019).

## 5. Conclusions and Discussion

In this work we selected a large sample of disc-like galaxies from the IllustrisTNG simulation to develop an algorithm capable of automatically classifying galaxies between lopsided and symmetric. Our main goal was to explore whether this classification can be accurately performed using only internal galactic parameters, thus neglecting information about their present-day environment.

To achieve this we employed the Random Forest algorithm, a machine learning approach that involves a supervised training process. To label our data as lopsided and symmetric galaxies we employed a Fourier decomposition of the galaxies' stellar density distribution over the radial interval  $R_{50} - 1.4R_{90}$ . We computed a radially average power of the  $m = 1$  mode,  $A_1$  within this range. Galaxies with  $A_1 > 0.1$  were classified as lopsided, and the remaining as symmetric. Our sample results in a total 5,273 lopsided and 2,646 symmetric galaxies. To avoid problems in the classification process due to the imbalanced nature of the dataset, we employed two variations of the RF algorithm: i) we used SMOTE to oversample symmetric galaxies in the training set, thus evening both classes, and ii) we used the BRF algorithm, which balances both classes on each tree by only bootstrapping the minority class while undersampling the majority. Based on the considered metrics, we selected SMOTE+RF as the best model. The classification resulted in a total of 1,922 and 455 correctly and incorrectly classified. This translates in a balanced accuracy of accurate classification rate of  $\approx 80\%$  of both classes. To interpret and understand the different decisions leading the RF to the classification, we used a method to quantify "features importance". In particular we utilized an algorithm that randomly permutes features' values and calculates the decrease in a certain metric; which in our case we choose balanced-accuracy. We found that, to distinguish between both classes, the three most important parameters for the model are  $\mu_*$ ,  $T_p$ , and  $SFR$ . The excellent results obtained by our classifier, trained with features that do not account for the galaxies environment, strongly supports the hypothesis that lopsidedness is mainly a tracer of galaxies internal structures.

Even though our classifier demonstrated a very good performance, we find that  $\approx 20\%$  of the galaxies were misclassified. To study the misclassified cases, we first explore the distribution of the main parameters used by the RF. First, we find that the  $A_1$  value of the misclassified cases lies very close to the threshold used to label galaxies as lopsided or symmetric. As a result, these cases are typically associated to "borderline classifications" by  $A_1$ . Interestingly, we find that the distribution of the most important parameters, such as  $\mu_*$  and  $T_p$  are in good agreement with class they have been associated to by the RF algorithm. In other words, galaxies classified by  $A_1$  as lopsided, but as symmetric by the RF, have large  $\mu_*$  and  $T_p$  values. Conversely, galaxies classified by  $A_1$  as symmetric, but as lopsided by the RF, have low  $\mu_*$  and  $T_p$  values.

To further explore why galaxies with large central surface density and strongly cohesive present perturbed outer disk region, we selected a representative case. We find that the selected galaxy became a satellite of a more massive host  $\approx 1.7$  Gyr ago. Previous to the crossing of host virial radius, the galaxy had a symmetric configuration. However, shortly after its first pericentric passage its outer regions become perturbed due to the strong tidal interaction. Such strong and recent interaction induced a temporary lopsided perturbation on this galaxy. We find that 28% of this misclassified class are either satellites of a more massive host, or have had a very recent strong tidal interactions with a massive companion ( $>1:20$ ). For the other misclassified cases, other mechanism, such as asymmetric gas accretion, must be considered to explain the classifications. We will further explore this in a follow up analyses. In the case of galaxies with low  $\mu_*$  and  $T_p$  misclassified as symmetric by the RF algorithm, we find that, typically, they have not experienced recent significant interactions with massive companions. Thus, even though they are susceptible to develop a lopsided perturbation, no external interaction have triggered its onset.

Several parameters considered in this work as features require additional modeling to be estimated. Considering the advent of several surveys such as S-PLUS (Mendes de Oliveira et al. 2019), J-PAS (Benitez et al. 2014), and the LSST (Ivezić et al. 2019), we explored whether the performance of our classifier significantly drops when considering features that can be readily obtained from multi-band photometric surveys. In particular, we replace stellar mass estimates with their corresponding luminosity in the r-band, and dropped parameters such as  $T_p$  that involve dynamical modeling to estimate the total galaxy mass within  $R_{50}$ . Interestingly, we find the performance of our modeling is very mildly affected, with recovery rates of  $\approx 78\%$ . These results are very promising, as our algorithm could allow us to rapidly extract samples of lopsided galaxies from large surveys, allowing us to explore whether lopsidedness in present-day disc galaxies is connected to their specific evolutionary histories, which shaped their distinct internal properties (Dolfi et al. 2023).

*Acknowledgements.* V.F., F.A.G., and A.D. acknowledges support from ANID FONDECYT Regular 1211370, the ANID Basal Project FB210003, and the HORIZON-MSCA-2021-SE-01 Research and innovation programme under the Marie Skłodowska-Curie grant agreement number 101086388. This article is based on the research for the master's thesis to obtain the title of MSc in Astronomy at the University of La Serena. V.F. acknowledges the partial financial support of DIDULS through the project PTE2353855. V.F. also thanks Cristian Vega Martinez for his support on an early version of this project.

## References

- Aguirre, C., Pichara, K., & Becker, I. 2019, MNRAS, 482, 5078  
 Appleby, S., Davé, R., Sorini, D., Lovell, C. C., & Lo, K. 2023, MNRAS, 525, 1167  
 Aumer, M., White, S. D. M., Naab, T., & Scannapieco, C. 2013, MNRAS, 434, 3142  
 Baldwin, J. E., Lynden-Bell, D., & Sancisi, R. 1980, MNRAS, 193, 313  
 Ball, N. M., Loveday, J., Fukugita, M., et al. 2004, MNRAS, 348, 1038  
 Baron, D. & Poznanski, D. 2017, MNRAS, 465, 4530  
 Benitez, N., Dupke, R., Moles, M., et al. 2014 [arXiv: 1403.5237]  
 Bournaud, F., Combes, F., Jog, C. J., & Puerari, I. 2005, A&A, 438, 507  
 Bowyer, K. W., Chawla, N. V., Hall, L. O., & Kegelmeyer, W. P. 2011, CoRR, abs/1106.1813 [1106.1813]  
 Breiman, L. 1996, Machine Learning, 24, 123  
 Breiman, L. 2001, Machine Learning, 45, 5  
 Carliles, S., Budavári, T., Heinis, S., Priebe, C., & Szalay, A. S. 2010, ApJ, 712, 511  
 Cenarro, A. J., Moles, M., Cristóbal-Hornillos, D., et al. 2019, A&A, 622, A176  
 Chen, C. & Breiman, L. 2004, University of California, Berkeley  
 Cheng, T.-Y., Li, N., Conselice, C. J., et al. 2020, MNRAS, 494, 3750  
 Conselice, C. J. 2014, ARA&A, 52, 291  
 Conselice, C. J., Bershady, M. A., & Jangren, A. 2000, ApJ, 529, 886  
 Cover, T. & Hart, P. 1967, IEEE Transactions on Information Theory, 13, 21  
 Dieleman, S., Willett, K. W., & Dambre, J. 2015, MNRAS, 450, 1441  
 Dolfi, A., Gómez, F. A., Monachesi, A., et al. 2023, MNRAS, 526, 567  
 Erwin, P. 2019, MNRAS, 489, 3553  
 Farias, H., Ortiz, D., Damke, G., Jaque Arancibia, M., & Solar, M. 2020, Astronomy and Computing, 33, 100420  
 Friedman, J. H. 2001, Annals of statistics, 1189  
 Gao, D., Zhang, Y.-X., & Zhao, Y.-H. 2009, Research in Astronomy and Astrophysics, 9, 220  
 Genel, S., Vogelsberger, M., Springel, V., et al. 2014, MNRAS, 445, 175  
 Giles, D. & Walkowicz, L. 2019, MNRAS, 484, 834  
 Gómez, F. A., White, S. D. M., Marinacci, F., et al. 2016, MNRAS, 456, 2779  
 Guha, S., Rastogi, R., & Shim, K. 2000, Information Systems, 25, 345  
 Guzmán-Ortega, A., Rodríguez-Gómez, V., Snyder, G. F., Chamberlain, K., & Hernquist, L. 2023, MNRAS, 519, 4920  
 Hocking, A., Geach, J. E., Sun, Y., & Davey, N. 2018, MNRAS, 473, 1108  
 Huertas-Company, M., Gravet, R., Cabrera-Vives, G., et al. 2015, ApJS, 221, 8  
 Ivezić, Ž., Kahn, S. M., Tyson, J. A., et al. 2019, ApJ, 873, 111  
 Jog, C. J. 1997, ApJ, 488, 642  
 Jog, C. J. 2002, A&A, 391, 471  
 Jog, C. J. & Combes, F. 2009, Phys. Rep., 471, 75  
 Jolliffe, I. T. 2002, Principal Component Analysis, 2nd edn. (Springer)  
 Joshi, G. D., Pillepich, A., Nelson, D., et al. 2020, MNRAS, 496, 2673  
 Kauffmann, G., Heckman, T. M., White, S. D. M., et al. 2003, MNRAS, 341, 33



- Kennicutt, Robert C., J. 1998, *ARA&A*, 36, 189
- Kollmeier, J., Anderson, S. F., Blanc, G. A., et al. 2019, in *Bulletin of the American Astronomical Society*, Vol. 51, 274
- Lagos, C. d. P., Theuns, T., Stevens, A. R. H., et al. 2017, *MNRAS*, 464, 3850
- Lee, J. & Shin, M.-S. 2021, *AJ*, 162, 297
- Lloyd, S. 1982, *IEEE Transactions on Information Theory*, 28, 129
- Lokas, E. L. 2022, *A&A*, 662, A53
- Mendes de Oliveira, C., Ribeiro, T., Schoenell, W., et al. 2019, *MNRAS*, 489, 241
- Monsalves, N., Jaque Arancibia, M., Bayo, A., et al. 2024, arXiv e-prints, arXiv:2408.11960
- Mucesh, S., Hartley, W. G., Palmese, A., et al. 2021, *MNRAS*, 502, 2770
- Nelson, D., Pillepich, A., Genel, S., et al. 2015, *Astronomy and Computing*, 13, 12
- Nelson, D., Pillepich, A., Springel, V., et al. 2019a, *MNRAS*, 490, 3234
- Nelson, D., Pillepich, A., Springel, V., et al. 2019b, *MNRAS*, 490, 3234
- Nelson, D., Pillepich, A., Springel, V., et al. 2018, *MNRAS*, 475, 624
- Nelson, D., Springel, V., Pillepich, A., et al. 2019c, *Computational Astrophysics and Cosmology*, 6, 2
- Noordermeer, E., Sparke, L. S., & Levine, S. E. 2001, *MNRAS*, 328, 1064
- O’Shea, K. & Nash, R. 2015, arXiv e-prints, arXiv:1511.08458
- Phookun, B., Vogel, S. N., & Mundy, L. G. 1993, *ApJ*, 418, 113
- Pillepich, A., Nelson, D., Springel, V., et al. 2019a, *MNRAS*, 490, 3196
- Pillepich, A., Nelson, D., Springel, V., et al. 2019b, *MNRAS*, 490, 3196
- Pillepich, A., Springel, V., Nelson, D., et al. 2018, *MNRAS*, 473, 4077
- Planck Collaboration, Ade, P. A. R., Aghanim, N., et al. 2016, *A&A*, 594, A13
- Reichard, T. A., Heckman, T. M., Rudnick, G., Brinchmann, J., & Kauffmann, G. 2008, *ApJ*, 677, 186
- Reichard, T. A., Heckman, T. M., Rudnick, G., et al. 2009, *ApJ*, 691, 1005
- Richter, O. & Sacisi, R. 1994, *Astronomy & Astrophysics*, 290, L9
- Rudnick, G. & Rix, H.-W. 1998, *AJ*, 116, 1163
- Rudnick, G., Rix, H.-W., & Kennicutt, Robert C., J. 2000, *ApJ*, 538, 569
- Rumelhart, D. E. & McClelland, J. L. 1987, *Learning Internal Representations by Error Propagation* (MIT Press), 318–362
- Sánchez-Sález, P., Reyes, I., Valenzuela, C., et al. 2021, *AJ*, 161, 141
- Sarkar, J., Bhatia, K., Saha, S., Safonova, M., & Sarkar, S. 2022, *MNRAS*, 510, 6022
- Sellwood, J. A. 2013, in *Planets, Stars and Stellar Systems. Volume 5: Galactic Structure and Stellar Populations*, ed. T. D. Oswalt & G. Gilmore, Vol. 5, 923
- Springel, V. 2010, *MNRAS*, 401, 791
- van Eymeren, J., Jütte, E., Jog, C. J., Stein, Y., & Dettmar, R. J. 2011, *A&A*, 530, A30
- Varela-Lavin, S., Gómez, F. A., Tissera, P. B., et al. 2023, *MNRAS*, 523, 5853
- Vogelsberger, M., Genel, S., Springel, V., et al. 2014, *Nature*, 509, 177
- Walker, I. R., Mihos, J. C., & Hernquist, L. 1996, *ApJ*, 460, 121
- Weinberg, M. D. 1994, *ApJ*, 421, 481
- Zaritsky, D. & Rix, H.-W. 1997, *ApJ*, 477, 118
- Zaritsky, D., Salo, H., Laurikainen, E., et al. 2013, *ApJ*, 772, 135
- Zhang, Y., Ma, H., Peng, N., Zhao, Y., & Bing Wu, X. 2013, *The Astronomical Journal*, 146, 22